Geophysical Journal International

Geophys. J. Int. (2025) **243,** 1–18
Advance Access publication 2025 August 18
Research Paper

https://doi.org/10.1093/gji/ggaf310

Analysis of fingerprint-derived geocentre motion time-series using multichannel singular spectrum analysis

Hongjuan Yu,[1] Yong Zhang,[1] Yu Sun ,[2] Krzysztof Sośnica[3] and Yi Shen[4]

[1] *School of Geomatics, Liaoning Technical University, Fuxin* 123000*, China*
[2] *Key Lab of Spatial Data Mining and Information Sharing, Ministry of Education, Fuzhou University, Wulongjiang North Road, Fuzhou* 350108 *Fujian, China. E-mail: jade.yusun@outlook.com*
[3] *Institute of Geodesy and Geoinformatics, Wrocław University of Environmental and Life Sciences, Grunwaldzka* 53, PL-50-357 *Wrocław, Poland*
[4] *School of Geographic Sciences, Xinyang Normal University, Xinyang 464000, China*

Accepted 2025 August 10. Received 2025 August 10; in original form 2025 March 20

SUMMARY

Understanding the geophysical drivers of seasonal geocentre motion (GCM) variations remains challenging due to the complexity of Earth system interactions, limited data on individual mass redistribution components and model uncertainties. This study presents a comprehensive investigation of seasonal GCM signals from April 2002 to January 2024 using the Fingerprint Approach (FPA), which enables direct quantification of contributions from distinct Earth system components. Additionally, Multichannel Singular Spectrum Analysis (MSSA) is applied to quantify the influence of terrestrial water storage (TWS), atmosphere (ATM) and ocean (OCN) variability on seasonal GCM fluctuations. Correlation and lag analyses are employed to explore their temporal relationships and underlying geophysical linkages. The results reveal that TWS, ATM and OCN jointly explain 97.9 per cent, 98.1 per cent and 90.8 per cent of the seasonal variance in the X, Y and Z components of GCM, respectively. TWS exerts as the dominant contributor in the Y (66.4 per cent) and Z (67.9 per cent) components, while ATM and OCN each contribute less than 49 per cent to all components. Further analysis indicates that ATM, OCN and TWS exhibit varying lag relationships with GCM in the X and Z components, while TWS demonstrates a notably stronger correlation with GCM in the Y component. Importantly, an approximately 120-d periodic signal identified in GCM is, for the first time, linked to global precipitation variability, providing a novel geophysical interpretation. These findings enhance our understanding of climate-driven geophysical mass redistribution and offer new insights into the processes governing seasonal GCM variations.

Key words: Global change from geodesy; Reference systems; Satellite geodesy; Satellite gravity; Time variable gravity; Time-series analysis.

1 INTRODUCTION

Earth's surface mass undergoes continuous spatiotemporal variations driven by both external and internal geophysical processes (Wu *et al.* 2006; Tapley *et al.* 2019; Nie *et al.* 2025). On seasonal timescales, these variations reflect dynamic interactions among three key components: terrestrial water storage (TWS), the atmosphere (ATM) and the oceans (OCN), significantly influencing Earth's mass distribution (Bouillé *et al.* 2000; Crétaux *et al.* 2002; Liu *et al.* 2024). These mass redistributions not only alter Earth's gravity field but also have profound implications for global climate change (Chen *et al.* 2019; Tapley *et al.* 2019). Geocentre motion (GCM) is typically defined as the relative movement of the Earth's centre of mass (CM) with respect to the centre of figure (CF) of the solid Earth (Dong *et al.* 2003; Guo *et al.* 2008; Wu *et al.* 2012; Zannat & Tregoning 2017; Yu *et al.*, 2025a), reflecting the complex processes of mass redistribution within the Earth system. Neglecting GCM in mass balance estimates can lead to significant errors, particularly in large-scale ocean mass variation assessments (Chambers *et al.* 2004; Bury *et al.* 2025). Moreover, seasonal variations in GCM play a crucial role in the terrestrial reference frame realization (Haines *et al.* 2024; Rebischung *et al.* 2024), polar motion observations (Zajdel *et al.* 2019) and geodynamic studies (Kuang *et al.* 2015).

Global mass changes arise from a combination of factors, including precipitation distribution, atmospheric circulation and ocean currents. Chen *et al.* (1996) first identified a ∼120-d periodic signal in global precipitation variability, providing a crucial reference for validating and

improving hydrological models. As a fundamental driver of the hydrological cycle (Eltahir & Bras 1996; Trenberth *et al.* 2003; Fallah *et al.* 2020), precipitation plays a significant role in sub-seasonal to seasonal variations in TWS (Guo *et al.* 2018). Nastula *et al.* (2011) further established a strong correlation between the 120-d signal and short-term polar motion excitation, primarily driven by global mass redistribution associated with atmospheric angular momentum and ocean currents. In the mid-latitude regions of the Northern Hemisphere, seasonal climate variations on this timescale are mainly influenced by atmospheric circulation and sea surface temperature anomalies, particularly during winter, leading to the emergence of a 120-d mid-latitude seasonal oscillation (Stan & Krishnamurthy 2019; Manthos *et al.* 2022; Stan 2022). While these studies provide valuable insights into the origin of the 120-d periodic signal, its underlying geophysical causes in relation to GCM variations remain inadequate and require further investigation.

The GRACE satellite mission revolutionized the study of time-variable gravity fields, significantly improving the accuracy and resolution of mass change assessments (Tapley *et al.* 2004; Yu *et al.* 2025b). However, GRACE-derived gravity field models exclude first-degree terms, which correspond to GCM variations. To address this limitation, Swenson *et al.* (2008) combined GRACE gravity solutions with ocean bottom pressure (OBP) models to estimate first-degree spherical harmonic (SH) coefficients. Despite its innovation, this method failed to fully account for issues such as land-ocean signal leakage and self-attraction and loading (SAL) effects (Tamisiea *et al.* 2010), leading to an underestimation of GCM amplitudes in the X and Z components. Importantly, the SAL effects have a significant influence on the annual variation of GCM (Clarke *et al.* 2005; Sun *et al.* 2023). To overcome these limitations, Sun *et al.* (2016) developed an optimized method that enables the simultaneous estimation of both first-degree SH coefficients and the C_{20} coefficient, thereby improving GCM assessments. Additionally, the Earth's first-degree SH coefficients can also be derived using satellite laser ranging (SLR) techniques, including the network translation method (Sośnica *et al.* 2015; Yu *et al.* 2021) and the dynamic method (Ries 2016; Cheng 2024). However, these methods do not directly isolate the contributions of individual geophysical components to GCM, limiting further analysis of the driving factors behind its seasonal variations.

The Fingerprint Approach (FPA) provides an effective solution to this challenge (Rietbroek *et al.* 2012, 2016; Sun *et al.* 2019) by modelling global mass redistribution through pre-defined regional mass variation patterns ('fingerprints'). In the CF reference frame, the Earth's surface is divided into regions, with fingerprints calculated based on the sea level equation (Tamisiea *et al.* 2010). By superimposing regional mass variations, the FPA constructs a global mass variation model that effectively estimates the first-degree SH terms caused by mass redistribution. Additionally, the FPA accounts for self-attraction and loading (SAL) effects while simultaneously quantifying the contributions of various geophysical components to the GCM. Before solving GRACE gravity field models, the AOD-1B product is commonly used as a background model to filter out high-frequency signals associated with atmospheric and oceanic mass changes (Dobslaw *et al.* 2017). While this reduces aliasing effects in gravity field solutions, it excludes atmospheric and oceanic (AO) contributions from the FPA-derived GCM components. To fully analyse the drivers of seasonal GCM signals, AO contributions must be incorporated into the FPA-derived GCM components to produce a complete GCM time-series. Specifically, the ATM, OCN and TWS variations affect seasonal GCM differently across the X, Y and Z components (Dong *et al.* 1997; Chen *et al.* 1999; Zhang & Sun 2018). Understanding these contributions comprehensively is essential for identifying the seasonal drivers of GCM.

This study systematically explores the contributions of the TWS, ATM and OCN components to seasonal GCM signals using the FPA. We conducted a comparative analysis of GCM, ATM, OCN and TWS time-series to examine their correlations and lag relationships. To enhance signal extraction and investigate the seasonal interactions among the X, Y and Z components of GCM, we employed Multichannel Singular Spectrum Analysis (MSSA), a powerful method for analysing multivariate geophysical time-series (Shen *et al.* 2021; Ji *et al.* 2023; Aliabad *et al.* 2024). MSSA was also used to analyse the seasonal amplitude and phase relationships of the GCM, ATM, OCN and TWS series, uncovering strong consistency, particularly in the ∼120-d periodic signal, and supporting its potential geophysical origin. The study further evaluates the contributions of ATM, OCN and TWS to FPA-derived GCM, confirming their roles as key drivers of seasonal GCM signals. These findings provide valuable insights into the geophysical drivers of seasonal GCM variations and lay a strong foundation for future research in this area.

2 METHODOLOGY AND DATA SETS

2.1 Fingerprint approach

The FPA (Sun *et al.* 2019) defines the global mass redistribution pattern resulting from regional mass changes as a fingerprint $\boldsymbol{f}^M$. By superimposing the mass changes caused by migration in each region, the global mass redistribution $\boldsymbol{g}^{\mathrm{M}}$ can be expressed as follows:

$$\underset{n\times 1}{\boldsymbol{g}^M} = \underset{n\times w}{\boldsymbol{F}^M}\ \underset{w\times 1}{\boldsymbol{a}}, \tag{1}$$

where $\boldsymbol{F}^M$ is a set of fingerprints $\boldsymbol{f}^M$, the superscript M denotes variables associated with the fingerprint, w is the number of fingerprints, n is the number of SH coefficients and $\boldsymbol{a}$ is the fingerprint coefficient vector.

The mass coefficients can be derived by converting the Stokes coefficient from the GRACE gravity field model as follows:

$$\begin{Bmatrix} \boldsymbol{g}^M \\ \boldsymbol{f}^M \end{Bmatrix} = \frac{\alpha\rho(2l+1)}{3(1+k_l)} \begin{Bmatrix} \boldsymbol{g} \\ \boldsymbol{f} \end{Bmatrix}, \tag{2}$$

where α is the Earth's mean radius, ρ is the Earth's mean density, l is the degree and k_l is the load Love number. Then eq. (1) can be transformed into:

$$\underset{n\times 1}{\boldsymbol{g}} = \underset{n\times w}{\boldsymbol{F}}\ \underset{w\times 1}{\boldsymbol{a}}, \tag{3}$$

where $\boldsymbol{F}$ is a set of fingerprints $\boldsymbol{f}$, and it is obtained by the transformation of $\boldsymbol{f}^M$ in each region. $\boldsymbol{g}$ is provided by the GRACE gravity field SH coefficients starting from C_{21}. However, the degree-1 SH coefficients are missing and the C_{20} coefficient is not accurate in GRACE solutions. Therefore, the above equation should be written as:

$$\underset{(n-4)\times 1}{\boldsymbol{g}} = \underset{(n-4)\times n}{\boldsymbol{T}}\ \underset{n\times w}{\boldsymbol{F}}\ \underset{w\times 1}{\boldsymbol{a}} \tag{4}$$

$$\boldsymbol{T} = \begin{bmatrix} 0 & 0 & 0 & 0 & 1 & 0 & \cdots & \cdots & 0 \\ 0 & 0 & 0 & 0 & 0 & 1 & \ddots & \ddots & \vdots \\ \vdots & \vdots & \vdots & \vdots & \vdots & \ddots & \ddots & \ddots & \vdots \\ \vdots & \vdots & \vdots & \vdots & \vdots & \ddots & \ddots & 1 & 0 \\ 0 & 0 & 0 & 0 & 0 & \cdots & \ddots & 0 & 1 \end{bmatrix}, \tag{5}$$

where $\boldsymbol{T}$ represents a truncation matrix used to eliminate the degree-1 coefficients and C_{20} from $\boldsymbol{F}$, ensuring consistency with the coefficients in $\boldsymbol{g}$.

The specific form of eq. (4) can be further expanded as:

$$\underbrace{\begin{bmatrix} C_{21} \\ S_{21} \\ C_{22} \\ \vdots \\ C_{lm} \\ S_{lm} \end{bmatrix}}_{\boldsymbol{g}} = \underbrace{\begin{bmatrix} C_{21}^{f^1} & C_{21}^{f^2} & C_{21}^{f^3} & \cdots & C_{21}^{f^w} \\ S_{21}^{f^1} & S_{21}^{f^2} & S_{21}^{f^3} & \cdots & S_{21}^{f^w} \\ C_{22}^{f^1} & C_{22}^{f^2} & C_{22}^{f^3} & \cdots & C_{22}^{f^w} \\ \vdots & \vdots & \vdots & \ddots & \vdots \\ C_{lm}^{f^1} & C_{lm}^{f^2} & C_{lm}^{f^3} & \cdots & C_{lm}^{f^w} \\ S_{lm}^{f^1} & S_{lm}^{f^2} & S_{lm}^{f^3} & \cdots & S_{lm}^{f^w} \end{bmatrix}}_{\boldsymbol{TF}} \underbrace{\begin{bmatrix} a^{f^1} \\ a^{f^2} \\ a^{f^3} \\ \vdots \\ a^{f^w} \end{bmatrix}}_{\boldsymbol{a}}, \tag{6}$$

where the fingerprints in $\boldsymbol{TF}$ can be calculated from the sea level equation (Tamisiea *et al.* 2010). To facilitate the understanding of eq. (6), we have added a specific example in the Supplementary Information, illustrating the application of the fingerprint approach in jointly solving for degree-1 terms and the C_{20} coefficient.

The vector $\boldsymbol{a}$ is estimated by the least-squares method as:

$$\boldsymbol{a} = (\boldsymbol{F}^T \boldsymbol{T}^T \boldsymbol{P} \boldsymbol{T} \boldsymbol{F})^{-1} \boldsymbol{F}^T \boldsymbol{T}^T \boldsymbol{P} \boldsymbol{g}, \tag{7}$$

where $\boldsymbol{P}$ is the weight matrix, with its elements inversely proportional to the variance of the calibration errors in the GRACE SH coefficients (Sun *et al.* 2019).

In this study, we define five types of fingerprints of Earth's mass redistribution, including the Antarctic (ANT) and Greenland (GRE) ice sheets, continental glaciers (GLA), TWS and glacial isostatic adjustment (GIA). Eq. (6) can be explicitly expressed as:

$$\boldsymbol{g} = \underbrace{[\boldsymbol{U}_1, \boldsymbol{U}_2, \boldsymbol{U}_3, \boldsymbol{U}_4, \boldsymbol{U}_5]}_{\boldsymbol{TF}} [\boldsymbol{a}_1, \boldsymbol{a}_2, \boldsymbol{a}_3, \boldsymbol{a}_4, \boldsymbol{a}_5]^T \tag{8}$$

$$\boldsymbol{g} = \begin{bmatrix} C_{21} & S_{21} & C_{22} & \cdots & C_{lm} & S_{lm} \end{bmatrix}^T \tag{9}$$

$$\boldsymbol{U}_1 = \begin{bmatrix} C_{21}^{ANT^1} & C_{21}^{ANT^2} & \cdots & C_{21}^{ANT^p} \\ S_{21}^{ANT^1} & S_{21}^{ANT^2} & \cdots & S_{21}^{ANT^p} \\ C_{22}^{ANT^1} & C_{22}^{ANT^2} & \cdots & C_{22}^{ANT^p} \\ \vdots & \vdots & \vdots & \vdots \\ C_{lm}^{ANT^1} & C_{lm}^{ANT^2} & \cdots & C_{lm}^{ANT^p} \\ S_{lm}^{ANT^1} & S_{lm}^{ANT^2} & \cdots & S_{lm}^{ANT^p} \end{bmatrix}, \boldsymbol{U}_2 = \begin{bmatrix} C_{21}^{GRE^1} & C_{21}^{GRE^2} & \cdots & C_{21}^{GRE^q} \\ S_{21}^{GRE^1} & S_{21}^{GRE^2} & \cdots & S_{21}^{GRE^q} \\ C_{22}^{GRE^1} & C_{22}^{GRE^2} & \cdots & C_{22}^{GRE^q} \\ \vdots & \vdots & \vdots & \vdots \\ C_{lm}^{GRE^1} & C_{lm}^{GRE^2} & \cdots & C_{lm}^{GRE^q} \\ S_{lm}^{GRE^1} & S_{lm}^{GRE^2} & \cdots & S_{lm}^{GRE^q} \end{bmatrix},$$

$$\boldsymbol{U}_3 = \begin{bmatrix} C_{21}^{GLA^1} & C_{21}^{GLA^2} & \cdots & C_{21}^{GLA^r} \\ S_{21}^{GLA^1} & S_{21}^{GLA^2} & \cdots & S_{21}^{GLA^r} \\ C_{22}^{GLA^1} & C_{22}^{GLA^2} & \cdots & C_{22}^{GLA^r} \\ \vdots & \vdots & \vdots & \vdots \\ C_{lm}^{GLA^1} & C_{lm}^{GLA^2} & \cdots & C_{lm}^{GLA^r} \\ S_{lm}^{GLA^1} & S_{lm}^{GLA^2} & \cdots & S_{lm}^{GLA^r} \end{bmatrix}, \boldsymbol{U}_4 = \begin{bmatrix} C_{21}^{TWS^1} & C_{21}^{TWS^2} & \cdots & C_{21}^{TWS^s} \\ S_{21}^{TWS^1} & S_{21}^{TWS^2} & \cdots & S_{21}^{TWS^s} \\ C_{22}^{TWS^1} & C_{22}^{TWS^2} & \cdots & C_{22}^{TWS^s} \\ \vdots & \vdots & \vdots & \vdots \\ C_{lm}^{TWS^1} & C_{lm}^{TWS^2} & \cdots & C_{lm}^{TWS^s} \\ S_{lm}^{TWS^1} & S_{lm}^{TWS^2} & \cdots & S_{lm}^{TWS^s} \end{bmatrix}, \tag{10}$$

$$\boldsymbol{U}_5 = \begin{bmatrix} C_{21}^{GIA^1} & C_{21}^{GIA^2} & \cdots & C_{21}^{GIA^t} \\ S_{21}^{GIA^1} & S_{21}^{GIA^2} & \cdots & S_{21}^{GIA^t} \\ C_{22}^{GIA^1} & C_{22}^{GIA^2} & \cdots & C_{22}^{GIA^t} \\ \vdots & \vdots & \vdots & \vdots \\ C_{lm}^{GIA^1} & C_{lm}^{GIA^2} & \cdots & C_{lm}^{GIA^t} \\ S_{lm}^{GIA^1} & S_{lm}^{GIA^2} & \cdots & S_{lm}^{GIA^t} \end{bmatrix}$$

$$\begin{aligned} &\boldsymbol{a}_1 = \begin{bmatrix} a^{ANT^1} & a^{ANT^2} & \cdots & a^{ANT^P} \end{bmatrix}, \boldsymbol{a}_2 = \begin{bmatrix} a^{GRE^1} & a^{GRE^2} & \cdots & a^{GRE^q} \end{bmatrix}, \\ &\boldsymbol{a}_3 = \begin{bmatrix} a^{GLA^1} & a^{GLA^2} & \cdots & a^{GLA^r} \end{bmatrix}, \boldsymbol{a}_4 = \begin{bmatrix} a^{TWS^1} & a^{TWS^2} & \cdots & a^{TWS^s} \end{bmatrix}, \\ &\boldsymbol{a}_5 = \begin{bmatrix} a^{GIA^1} & a^{GIA^2} & \cdots & a^{GIA^t} \end{bmatrix} \end{aligned} \tag{11}$$

where $\boldsymbol{U}_1$, $\boldsymbol{U}_2$, $\boldsymbol{U}_3$, $\boldsymbol{U}_4$ and $\boldsymbol{U}_5$ denote the fingerprint gravity field contributions derived by solving the sea level equation (SLE) for each of the five categories (ANT, GRE, GLA, TWS, GIA). p, q, r, s and t represent the number of each of the five categories. $\boldsymbol{a}_1$, $\boldsymbol{a}_2$, $\boldsymbol{a}_3$, $\boldsymbol{a}_4$ and $\boldsymbol{a}_5$ represent the fingerprint coefficient vectors corresponding to the ANT, GRE, GLA, TWS and GIA, respectively.

After estimating the fingerprint coefficient vector $\boldsymbol{a}$, C_{10}, C_{11}, S_{11} and C_{20} can be further solved by:

$$\begin{bmatrix} C_{10} \\ C_{11} \\ S_{11} \\ C_{20} \end{bmatrix} = [\boldsymbol{V}_1, \boldsymbol{V}_2, \boldsymbol{V}_3, \boldsymbol{V}_4, \boldsymbol{V}_5][\boldsymbol{a}_1, \boldsymbol{a}_2, \boldsymbol{a}_3, \boldsymbol{a}_4, \boldsymbol{a}_5]^T \tag{12}$$

$$\boldsymbol{V}_1 = \begin{bmatrix} C_{10}^{ANT^1} & C_{10}^{ANT^2} & \cdots & C_{10}^{ANT^P} \\ C_{11}^{ANT^1} & C_{11}^{ANT^2} & \cdots & C_{11}^{ANT^P} \\ S_{11}^{ANT^1} & S_{11}^{ANT^2} & \cdots & S_{11}^{ANT^P} \\ C_{20}^{ANT^1} & C_{20}^{ANT^2} & \cdots & C_{20}^{ANT^P} \end{bmatrix}, \boldsymbol{V}_2 = \begin{bmatrix} C_{10}^{GRE^1} & C_{10}^{GRE^2} & \cdots & C_{10}^{GRE^q} \\ C_{11}^{GRE^1} & C_{11}^{GRE^2} & \cdots & C_{11}^{GRE^q} \\ S_{11}^{GRE^1} & S_{11}^{GRE^2} & \cdots & S_{11}^{GRE^q} \\ C_{20}^{GRE^1} & C_{20}^{GRE^2} & \cdots & C_{20}^{GRE^q} \end{bmatrix},$$

$$\boldsymbol{V}_3 = \begin{bmatrix} C_{10}^{GLA^1} & C_{10}^{GLA^2} & \cdots & C_{10}^{GLA^r} \\ C_{11}^{GLA^1} & C_{11}^{GLA^2} & \cdots & C_{11}^{GLA^r} \\ S_{11}^{GLA^1} & S_{11}^{GLA^2} & \cdots & S_{11}^{GLA^r} \\ C_{20}^{GLA^1} & C_{20}^{GLA^2} & \cdots & C_{20}^{GLA^r} \end{bmatrix}, \boldsymbol{V}_4 = \begin{bmatrix} C_{10}^{TWS^1} & C_{10}^{TWS^2} & \cdots & C_{10}^{TWS^s} \\ C_{11}^{TWS^1} & C_{11}^{TWS^2} & \cdots & C_{11}^{TWS^s} \\ S_{11}^{TWS^1} & S_{11}^{TWS^2} & \cdots & S_{11}^{TWS^s} \\ C_{20}^{TWS^1} & C_{20}^{TWS^2} & \cdots & C_{20}^{TWS^s} \end{bmatrix}, \tag{13}$$

$$\boldsymbol{V}_5 = \begin{bmatrix} C_{10}^{GIA^1} & C_{10}^{GIA^2} & \cdots & C_{10}^{GIA^t} \\ C_{11}^{GIA^1} & C_{11}^{GIA^2} & \cdots & C_{11}^{GIA^t} \\ S_{11}^{GIA^1} & S_{11}^{GIA^2} & \cdots & S_{11}^{GIA^t} \\ C_{20}^{GIA^1} & C_{20}^{GIA^2} & \cdots & C_{20}^{GIA^t} \end{bmatrix},$$

where $\boldsymbol{V}_1$, $\boldsymbol{V}_2$, $\boldsymbol{V}_3$, $\boldsymbol{V}_4$ and $\boldsymbol{V}_5$ denote the set of coefficients corresponding to the degree-1 terms (C_{10}, C_{11}, S_{11}) and the degree-2 zonal term (C_{20}) for the five types of fingerprints of ANT, GRE, GLA, TWS and GIA.

2.2 MSSA

MSSA is a robust technique for extracting trends, oscillatory components and noise from multiple correlated time-series while also capturing their coupling relationships and spatiotemporal evolution. The method involves constructing multichannel time-lagged trajectory matrices, which are then combined into a joint matrix for singular value decomposition. The resulting principal components and associated eigenvectors are used to reconstruct the original signals (Zhang *et al.* 2021; Ji *et al.* 2023; Aliabad *et al.* 2024). In this study, MSSA is employed to jointly analyse GCM and the corresponding ATM, OCN and TWS time-series in the X, Y and Z components. This allows for the effective extraction and separation of dominant periodic signals specific to each contributing source.

2.3 Data set and data processing

This study utilizes GRACE/GRACE-FO Level-2 RL06.2 data, released by the Center for Space Research (CSR), covering the period from April 2002 to January 2024. The data set includes SH coefficients truncated at degree 60, with 33 missing monthly solutions. To remove the long-term solid Earth signal, the GIA model proposed by Peltier *et al*. (2018) is applied. Additionally, the monthly averaged AOD-1B product, which represents ATM and OCN mass variations, is embedded within the GAA and GAB components of the GRACE Level-2 product. By incorporating the first-degree terms from the GAA and GAB product, the atmospheric and oceanic signal component of GCM can be effectively extracted. Leveraging the de-aliasing correction method in GRACE gravity field data processing (Dobslaw *et al.* 2017), the first-degree terms are reintroduced into the GCM solutions derived from the FPA, restoring the atmospheric and oceanic mass variations that were removed during GRACE data processing. This procedure further enables a quantitative assessment of ATM and OCN contributions to seasonal GCM variability (https://icgem.gfz-potsdam.de/sl/temporal).

Recognizing precipitation as a key driver of seasonal and sub-seasonal variability in TWS, the study further analyses total precipitation data from two independent data sets: the European Centre for Medium-Range Weather Forecasts (ECMWF) ERA5 atmospheric reanalysis and the Global Precipitation Climatology Centre (GPCC). Both data sets cover the period from April 2002 to December 2023, providing a robust basis for evaluating precipitation-driven hydrological mass redistribution.

3 SEASONAL CHARACTERISTICS OF GEOCENTRE MOTION

3.1 Seasonal variation analysis

This study investigates the impact of ATM and OCN contributions on GCM by comparing FPA-derived GCM time-series before and after incorporating the ATM and OCN components. As illustrated in Fig. 1, the red curves represent the FPA-resolved GCM time-series in the X, Y and Z components, while the blue curves show the results after restoring the ATM and OCN effects, which are included in all subsequent FPA-based analyses. The results indicate notable seasonal variations in the GCM time-series, characterized by distinct trends that differ by component. The X component shows a relatively stable trend, whereas the Y component exhibits a positive trend, with notable upward shifts in 2010 and 2018. In contrast, the Z component displays a pronounced negative trend, primarily driven by the asymmetric glacier melt between the Northern and Southern Hemispheres, polar ice cap mass loss and the effects of GIA, while ocean coverage has a relatively minor influence

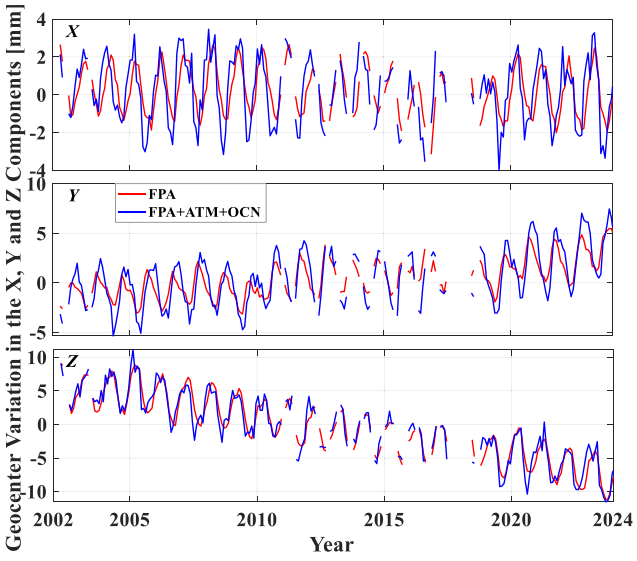

Figure 1. The GCM time-series resolved using the FPA.

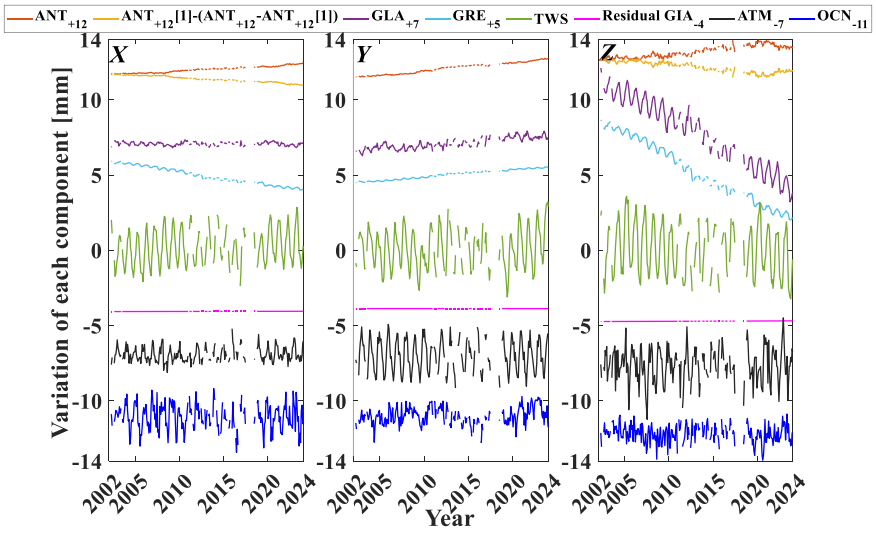

Figure 2. The various contributing components of the Earth system to the FPA-derived GCM.

on the trend (Zhang & Sun, 2018). Restoring the ATM and OCN components influences the seasonal fluctuations in all three components to varying degrees, but it does not alter their overall trends.

Fig. 2 illustrates the contributions of various geophysical components of the Earth system to GCM as resolved using the FPA. Given the limitations of the FPA in separating vertically superimposed signals, the ATM and OCN components used in this study are derived directly from the AOD-1B model to avoid potential uncertainties associated with FPA-derived estimates. Additionally, the ocean component in AOD-1B incorporates dynamic ocean variability, enhancing the comprehensiveness of the GCM driver analysis. The analysis reveals that seasonal variations in GCM are predominantly driven by TWS, ATM and OCN components, while in the Z component, contributions from GLA and GRE are also significant, though less than those from TWS, ATM and OCN components. The long-term trend component is primarily influenced by polar ice sheet loss, with the Z component exhibiting more pronounced changes compared to the X and Y components. Notably, apart from the Y component, the mass redistribution from the GRE and ANT exerts opposing effects on the GCM trend, with GRE having a significantly stronger impact than ANT. This discrepancy is primarily attributed to the greater mass loss of the GRE relative to the ANT (Sun *et al.* 2019). Furthermore, mass variations in ANT exhibit pronounced regional heterogeneity. While West Antarctica experiences substantial mass loss, some regions of East Antarctica are gaining mass due to increased snowfall. In contrast, the mass loss in GRE is more spatially concentrated, leading to a stronger influence on GCM (Otosaka *et al.* 2022; Pan *et al.* 2025). Although GIA contributes to the long-term GCM trend, the FPA-derived GCM solutions account for this effect by removing modelled GIA signals (Peltier *et al.*, 2018), resulting in only minor residual contributions to the GCM estimates. However, previous studies have noted instabilities in FPA-derived GIA estimates (Rietbroek 2014), underscoring the need for further methodological refinements. Given these limitations, this study primarily focuses on analysing the seasonal drivers of GCM rather than its long-term evolution.

The discontinuity of the GCM time-series presents challenges for seasonal signal analysis. To further explore the seasonal relationships among the ATM, OCN, TWS and GCM time-series, this study applies an iterative interpolation method combined with SSA to fill in missing data points (Kondrashov & Ghil 2006; Golyandina & Osipov 2007). All four time-series are detrended, and the results are shown in Fig. 3. The comparative analysis reveals that the detrended TWS series exhibits strong coherence with FPA-derived GCM across all three components (X, Y and Z), whereas ATM and OCN show relatively weaker consistency. Specifically, ATM demonstrates stronger correlations with GCM in the Y and Z components, while OCN exhibits better agreement in the X component. This directional asymmetry likely reflects the spatial sensitivity of GCM. The X component is primarily associated with ocean-covered regions, where oceanic mass variations exert a stronger influence. In contrast, the Y and Z components are more sensitive to atmospheric pressure loading over continental areas, amplifying the contribution of ATM in those components. Overall, the ATM, OCN and TWS signals exhibit notable agreement with the detrended GCM (denoted as FPA + ATM + OCN-Detrend in Fig. 3). To further validate this correlation, Fig. 3 also illustrates the superimposed time-series of ATM, OCN and TWS (i.e. ATM + OCN + TWS, represented by the yellow line). The comparison reveals that this combined signal shows a strong match with GCM in the X and Y components but a relatively weaker agreement in the Z component.

Two potential factors likely contribute to the discrepancies observed in the Z component. First, the seasonal contributions of glacial mass changes, particularly from GLA and GRE to GCM, exert a non-negligible influence on the Z-component variations, as indicated in Fig. 2. This is consistent with earlier findings (e.g. Zhang & Sun 2018), which highlighted the role of GRE in influencing Z-component seasonal variations. These findings indicate that the combined ATM + OCN + TWS time-series alone may not fully capture the detrended seasonal variations of GCM in this component. Secondly, clear phase offsets are present among ATM, OCN and TWS in the Z component, as evidenced in Fig. 3, where their respective peaks and troughs do not align temporally.

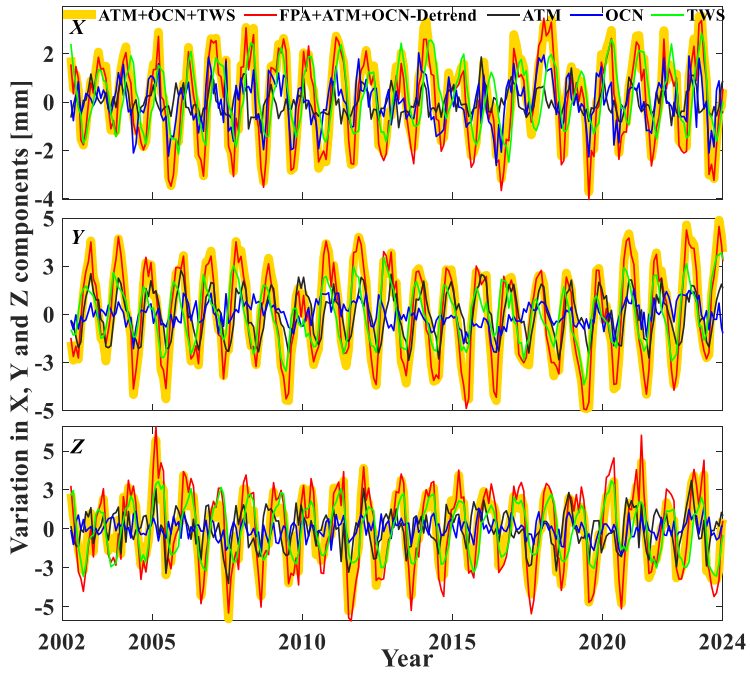

Figure 3. Comparison of detrended time-series of GCM with the contribution of various geophysical constituents.

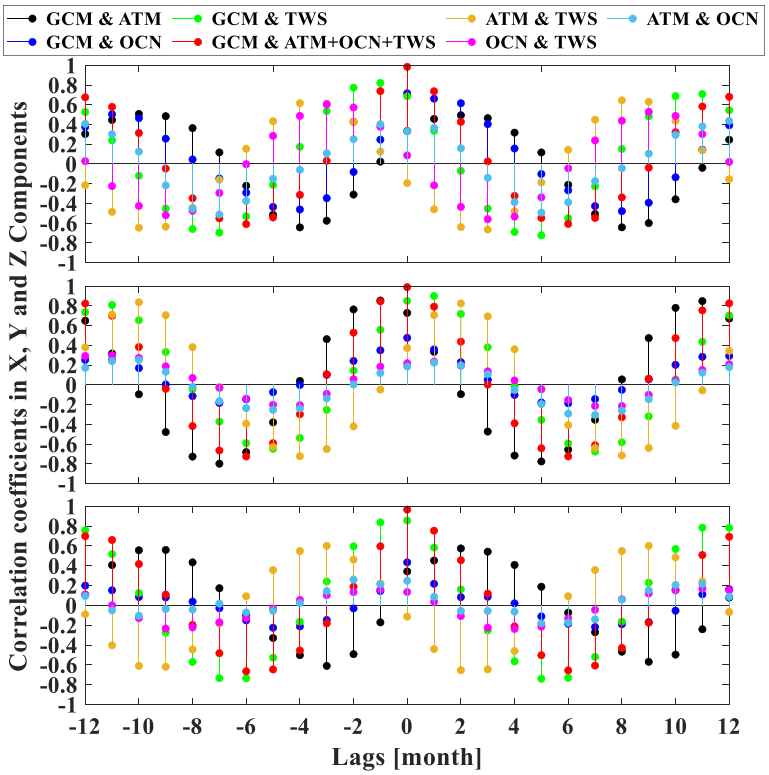

Figure 4. The correlation coefficients and lag times among ATM, OCN, TWS and FPA-based GCM after incorporating the ATM and OCN components.

3.2 Correlation and lag analysis

The observed misalignment among the ATM, OCN and TWS time-series provides an opportunity to further assess their individual and combined impacts on GCM (FPA + ATM + OCN-detrended in Fig. 3). To quantify these interactions, this study examines the correlation and lag relationships between GCM and each component (ATM, OCN and TWS), with detailed results summarized in Fig. 4 and Table 1.

Table 1. The correlation coefficients and lag times among ATM, OCN, TWS, AOT and FPA-based GCM after incorporating the ATM and OCN components (AOT = ATM + OCN + TWS).

		Maximum positive Correlation coefficient		Maximum negative Correlation coefficient	
Component	Time-series	Lag (month)	Correlation coefficient	Lag (month)	Correlation coefficient
X	GCM & ATM	+2	0.494	−4	−0.643
	GCM & OCN	0	0.716	−4	−0.462
	GCM & TWS	−1	0.821	+5	−0.723
	GCM & AOT	0	0.984	−6	−0.610
	ATM & TWS	−4	0.616	+3	−0.664
	OCN & TWS	−3	0.604	+3	−0.560
	ATM & OCN	−1	0.403	−7	−0.512
Y	GCM & ATM	−1	0.855	+5	−0.776
	GCM & OCN	0	0.477	+6	−0.186
	GCM & TWS	+1	0.902	+7	−0.675
	GCM & AOT	0	0.991	−6	−0.725
	ATM & TWS	+2	0.826	−4	−0.723
	OCN & TWS	+1	0.237	+7	−0.214
	ATM & OCN	+1	0.226	+7	−0.305
Z	GCM & ATM	+2	0.574	−3	−0.610
	GCM & OCN	0	0.434	−5	−0.225
	GCM & TWS	0	0.856	+5	−0.740
	GCM & AOT	0	0.966	-6	−0.665
	ATM & TWS	−3	0.601	+2	−0.654
	OCN & TWS	−1	0.159	+4	−0.237
	ATM & OCN	−2	0.262	+5	−0.181

The analysis reveals strong positive correlations between GCM and both ATM and TWS, accompanied by notable lags. Specifically, GCM lags ATM by approximately 1–2 month in all three components, with a peak correlation of 85.5 per cent at a 1-month lag in the Y component. GCM also lags TWS by up to 1 month, with positive correlation coefficients exceeding 82 per cent in all components, confirming the strong seasonal influence of TWS on GCM. In contrast, no clear lag is detected between GCM and OCN, although the highest correlation is found in the X component, underscoring the dominant role of oceanic mass variability in this component. Additionally, negative correlations between GCM and TWS are evident, peaking at approximately +5, +7 and +5 month in the X, Y and Z components, respectively, suggesting a delayed negative relationship. Further lag analysis reveals that ATM and OCN both lead TWS by 1–4 month in the X and Z components. This likely reflects the faster response of the ocean–atmosphere system to pressure and circulation anomalies, while TWS reflects slower land hydrology processes that influence GCM with a delay. The phase offsets among ATM, OCN and TWS are particularly evident in the X and Z components in Fig. 3.

Notably, the combined ATM + OCN + TWS series aligns more closely with GCM in the X component than in Z, highlighting the additional seasonal contributions of GRE and GLA to GCM in the Z component. As shown in Table 1, the combined ATM + OCN + TWS series achieves maximum correlations exceeding 96 per cent with GCM in all components, with no significant lag, demonstrating that this combined signal robustly captures the dominant seasonal variations of GCM.

Having identified ATM, OCN and TWS as the primary contributors to seasonal GCM variability and established their respective lag relationships, this study further investigates their amplitude and phase characteristics to provide deeper insights into the mass redistribution processes underlying seasonal GCM variations.

4 RESULTS AND SEASONAL SIGNAL DRIVING FACTORS

4.1 MSSA analysis of seasonal GCM variability

In signal analysis, MSSA is a powerful method for processing multivariate data, enhancing signal extraction and resolving complex interactions among system components. In this study, MSSA is employed to explore the interrelationships among the X, Y and Z components of GCM, providing a more comprehensive understanding of their seasonal variations and underlying geophysical drivers. Despite extensive research on seasonal signals in GCM, significant discrepancies in seasonal amplitude estimates remain, largely due to differences in computational and analytical methods (Kuang *et al.* 2019). To address this issue, this study applies MSSA with a window length of 9–10 yr to reconstruct the GCM, ATM, OCN and TWS, followed by spectral analysis using the Fast Fourier Transform (FFT). While MSSA may not always isolate purely single-frequency components, the dominant periodicities identified here demonstrate notable robustness and reliability, as evidenced by their agreement with prior studies (Kuang *et al.* 2019; Rebischung *et al.* 2024), results from spectral analysis, sensitivity tests on window length and evaluations of W-correlation.

Fig. 5 depicts a spectral comparison of seasonal signals derived from the GCM, ATM, OCN, TWS and combined ATM + OCN + TWS time-series. All time-series exhibit prominent annual and semi-annual signals, with the annual amplitude significantly exceeding that of the

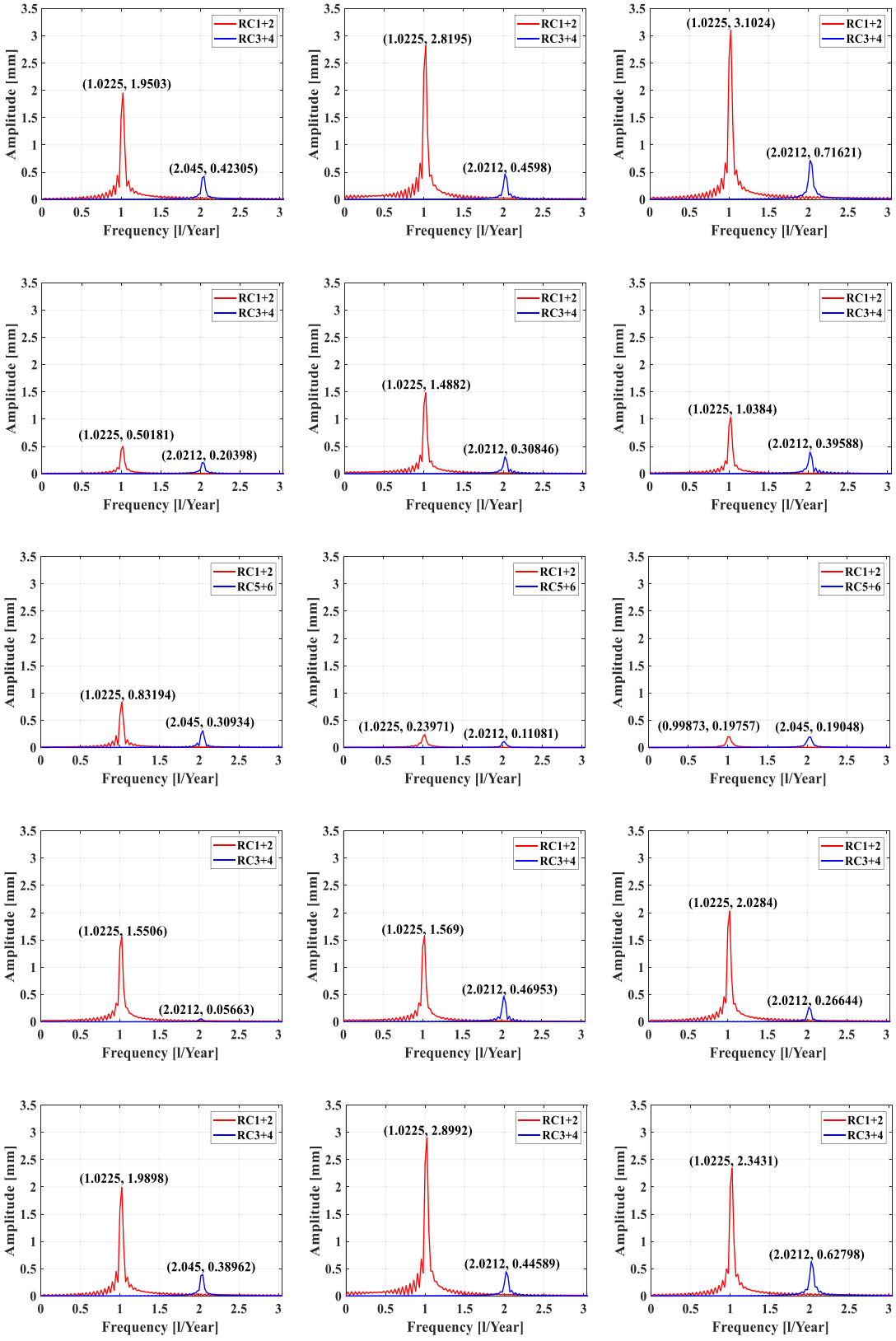

Figure 5. Annual and semi-annual spectrum analysis. The first row represents the X, Y and Z components of GCM (FPA + ATM + OCN-detrended); the second row corresponds to ATM; the third row depicts OCN; the fourth row illustrates TWS and the fifth row illustrates ATM + OCN + TWS. Values in parentheses indicate the frequency and amplitude.

Table 2. Annual and semi-annual amplitudes and phases, FPA + ATM + OCN-Detrend shows FPA-based GCM after incorporating the ATM and OCN component.

Component	Solutions	Annual		Semi-annual	
		Amplitude (mm)	Phase (°)	Amplitude (mm)	Phase (°)
X	FPA + ATM + OCN-Detrend	1.95 ± 0.08	58.7 ± 2.3	0.42 ± 0.08	295.3 ± 10.5
	ATM	0.50 ± 0.03	353.3 ± 3.1	0.20 ± 0.03	343.0 ± 7.0
	OCN	0.83 ± 0.06	13.4 ± 4.4	0.31 ± 0.06	269.2 ± 12.0
	TWS	1.55 ± 0.04	98.4 ± 1.3	0.06 ± 0.04	201.6 ± 34.1
	ATM + OCN + TWS	1.99 ± 0.08	59.0 ± 2.1	0.39 ± 0.09	292.7 ± 10.4
Y	FPA + ATM + OCN-Detrend	2.81 ± 0.08	321.7 ± 1.5	0.46 ± 0.08	160.4 ± 10.9
	ATM	1.50 ± 0.03	356.6 ± 1.2	0.31 ± 0.03	248.4 ± 5.4
	OCN	0.24 ± 0.05	326.7 ± 11.9	0.12 ± 0.05	72.8 ± 31.0
	TWS	1.57 ± 0.06	296.7 ± 2.0	0.47 ± 0.06	132.8 ± 10.7
	ATM + OCN + TWS	2.90 ± 0.08	325.4 ± 1.5	0.45 ± 0.08	164.0 ± 11.2
Z	FPA + ATM + OCN-Detrend	3.10 ± 0.10	63.3 ± 1.9	0.71 ± 0.10	251.8 ± 8.5
	ATM	1.04 ± 0.07	341.5 ± 3.8	0.40 ± 0.07	196.1 ± 9.8
	OCN	0.20 ± 0.05	26.6 ± 16.2	0.19 ± 0.05	298.5 ± 15.0
	TWS	2.03 ± 0.04	80.8 ± 1.2	0.27 ± 0.04	274.8 ± 9.1
	ATM + OCN + TWS	2.34 ± 0.10	51.3 ± 2.7	0.63 ± 0.10	243.3 ± 9.4

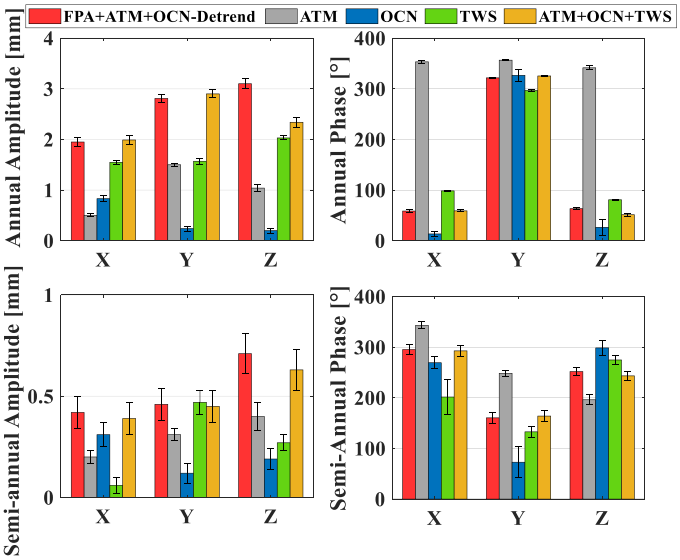

Figure 6. Annual and semi-annual amplitudes and phases of GCM.

semi-annual signal (Dong *et al.* 1997; Altamimi *et al.* 2023). Moreover, our analysis confirms that the amplitude of the FPA + ATM + OCN-detrended time-series is generally in good agreement with GCM estimates derived from CSR's SLR-based solutions, confirming the reliability of the FPA approach.

In the GCM spectra (first row), the Z component displays the largest annual amplitude among all three components, reflecting the significant redistribution of Earth's mass between the Northern and Southern Hemispheres along the Z-axis. In the ATM spectra (second row), the Y and Z components exhibit higher annual amplitudes than the X component, highlighting the dominant influence of atmospheric variations on GCM in these components. The OCN spectra (third row) show a pronounced annual peak in the X component, emphasizing the dominant role of ocean variation on GCM in this component. Similarly, the TWS spectra (fourth row) reveal a higher annual amplitude in the Z component compared to the X and Y components, reflecting the significant impact of global terrestrial hydrological processes on GCM along the Z-axis. In the combined ATM + OCN + TWS spectra (fifth row), the annual amplitudes in the X and Y components align closely with those of the GCM. However, a notable discrepancy is observed in the Z component, where the annual amplitude of GCM reaches 3.1024 mm, while ATM + OCN + TWS accounts for only 2.3431 mm. This difference is primarily attributed to the additional seasonal contributions from the GLA and GRE components, as discussed in Section 3.2. To quantify these effects, we detrended the Z-component time-series of GLA, GRE and FPA + ATM + OCN, and quantitatively evaluated their respective seasonal variance contributions. The results indicate that GLA and GRE contribute 24.7 per cent and 9.4 per cent, respectively, to the seasonal variance of the Z component, highlighting their notable roles in modulating GCM.

Table 2 provides a detailed comparison of the annual and semi-annual signals, along with an analysis of the seasonal characteristics of five time-series, as illustrated in Fig. 6. In the X and Y components, the annual amplitudes of GCM (red bars) closely align with those of

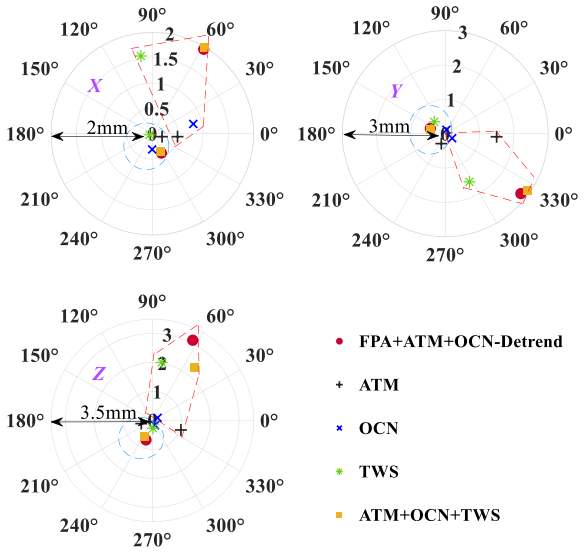

Figure 7. Phase and amplitude diagram of the annual (red dashed box) and semi-annual (blue dashed circles) signals in the five time-series.

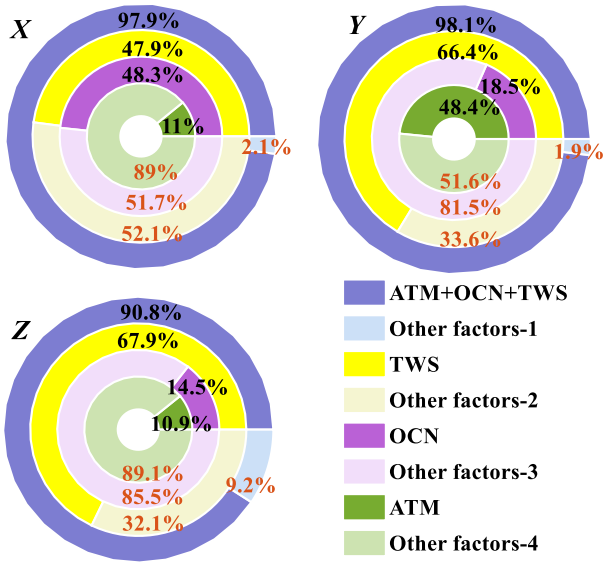

Figure 8. Contribution relationship of ATM, OCN, TWS and ATM + OCN + TWS to GCM.

ATM + OCN + TWS (yellow bars), whereas a slightly larger discrepancy is observed in the Z component. Regarding the annual signal phase, ATM and TWS exhibit closer alignment in the Y component, while more significant phase offsets are evident in the X and Z components. Notably, GCM and ATM + OCN + TWS demonstrate consistent phase behaviour across all three components. The semi-annual amplitude and phase patterns follow similar trends. The uncertainties in this study are estimated by fitting a rate-annual-semiannual model to the time-series, which may underestimate the actual errors. Future research should incorporate more robust error analysis methods to improve the seasonal signal accuracy.

To further illustrate these relationships, Fig. 7 presents a phase-amplitude distribution diagram. The results reveal strong clustering between GCM and ATM + OCN + TWS, reflecting their high consistency in seasonal signal patterns. In contrast, ATM, OCN and TWS exhibit more dispersed phase-amplitude distributions, with OCN showing greater variability than TWS.

4.2 Quantifying ATM, OCN and TWS contributions to seasonal GCM variability

Given the dominant roles of ATM, OCN and TWS as seasonal drivers of GCM, this study quantifies their individual and combined contributions to the total variance of FPA-derived GCM within the Earth's system components. As shown in Fig. 8, TWS is the largest contributor to seasonal GCM variations, accounting for 66.4 per cent and 67.9 per cent of the seasonal variance in the Y and Z components, respectively, and 47.9 per cent in the X component. In contrast, ATM and OCN contribute only 10.9 per cent and 14.5 per cent to the Z component, respectively, consistent with their relatively weak correlations with GCM in this component (57.4 per cent and 43.4 per cent; see Table 1). This

lower contribution in the Z component stems from the high-frequency signal interference in ATM, OCN and significant seasonal variations from GLA and GRE, which cannot be ignored. In the X and Y components, the combined contribution of ATM and OCN is comparable to, and slightly greater than, that of TWS. In contrast, TWS remains the dominant contributor to variance in the Z component. These results are broadly consistent with those reported by Zhang & Sun (2018), although their study found that ATM and OCN exerted a greater influence than TWS in the X and Y components. This discrepancy likely stems from their use of the GLDAS model, which excludes groundwater components, potentially underestimating total TWS contributions. In contrast, the FPA, which partitions Earth's surface and incorporates sea level equations, enables more accurate identification and quantification of TWS mass variations, particularly in capturing groundwater contributions.

Despite these differences, this study agrees that the combined ATM and OCN contributions to GCM variance are greater in the X and Y components than in the Z component. The combined ATM + OCN + TWS contributions account for 97.9 per cent, 98.1 per cent and 90.8 per cent of GCM variance in the X, Y and Z components, respectively. Notably, in the three components, the total variance explained by the individual contributions of ATM, OCN and TWS exceeds that of their combined signal (ATM + OCN + TWS). This discrepancy can be attributed to the intercomponent correlations and lag relationships, as summarized in Table 1. Specifically, ATM, OCN and TWS exhibit mutual lags of 1–4 month, and their phase misalignments can lead to partial signal cancellation when combined, thereby reducing the total variance.

In the Y component, both the variance explained by the combined ATM + OCN + TWS signal and the sum of their individual contributions exceed those in the X and Z components. This discrepancy may be attributed to the dominance of continental regions in the Y component and oceanic regions in the X component (Chen *et al.* 1999). TWS exerts a stronger influence on GCM than oceanic mass variations, and atmospheric loading is generally more pronounced over continents than oceans, both contributing to the greater variance observed in the Y component. In contrast, the relatively lower variance in the Z component may reflect the absence of contributions from the GLA and GRE components, which are known to significantly impact seasonal signals along the Z-axis, resulting in an underestimation of variance in this component.

In summary, seasonal oscillations in GCM are primarily influenced by mass redistribution associated with ATM, OCN and TWS processes.

4.3 Detection and interpretation of other periodic signals

To better isolate and identify periodic signals beyond the dominant annual and semi-annual components, this study applied MSSA to the FPA, ATM, OCN and TWS time-series, with the trends, annual and semi-annual signals removed. Fig. 9 presents the periodic signals detected by MSSA in the X, Y and Z components.

The analysis revealed periodic signals of approximately 3–5 yr and shorter period signals near 270 d across all four time-series. These signals are likely linked to distinct geophysical processes, although their specific origins require further investigation. Additionally, a ∼140-d periodic signal was detected in all three components of the ATM time-series. This signal is suspected to be an artefact arising from high-frequency atmospheric noise and was therefore not considered geophysically meaningful. Notably, a ∼160-d periodic signal was consistently observed in all three components of the FPA and TWS time-series. Further analysis of additional FPA-resolved components revealed weak ∼160-d signals in the GLA and GRE time-series. Previous studies (Chen *et al.* 2009; Cheng & Ries 2017; Yu *et al.* 2025a) have reported significant ∼160-d periodic signals in GRACE SH coefficients of degree and order no less than 2, attributing this signal to half of the nodal period of GRACE and GRACE-FO satellite orbits rather than a true geophysical phenomenon. As illustrated in eq. (6), FPA derives fingerprint coefficient vectors from high-degree GRACE SH coefficients, making it likely that this ∼160-d aliasing signal is inadvertently propagated into the TWS, GLA and GRE fingerprints. Recognizing this signal as a satellite-induced artefact, GRACE-based studies typically remove it to prevent contamination of geophysical interpretations in GCM analysis.

4.4 Significance of the ∼120-d periodic signal

Among the detected periodic signals, the ∼120-d periodic signal is particularly noteworthy, as it appears consistently in the GCM, ATM, OCN and TWS time-series (Fig. 9). This signal aligns with a growing body of literature reporting sub-seasonal periodicities in precipitation, TWS and snow water equivalent (Vishwakarma *et al.* 2021; Xue & Lau 2024; Zhu *et al.* 2025), all of which reflect surface mass redistribution processes. Given that precipitation is a key driver of both seasonal and subseasonal variations in TWS, this study further analyses precipitation data sets from ECMWF and GPCC. These data sets were converted into SH coefficients, from which degree-1 terms were extracted and transformed into GCM-equivalent components along the X, Y and Z axes (Fig. 10). The analysis reveals that precipitation fluctuations in the GPCC data set are consistently greater than those in the ECMWF data set across all three components. While the X and Y components of the two data sets display lower consistency, the Z component exhibits clear annual variability. MSSA analysis applied to both precipitation data sets confirms the presence of a ∼120-d periodic signal (Fig. 11). In Fig. 11, the spectral content of the GPCC total precipitation is shown in the bottom left panel, whereas the bottom right panel displays the corresponding spectrum from the ECMWF data set. Notably, although the ∼120-d signal is present in both data sets, the amplitude of this signal is consistently higher in GPCC than in ECMWF data. This discrepancy may be attributed to potential biases in ECMWF reanalysis products in regions with sparse observations, despite their global coverage. In

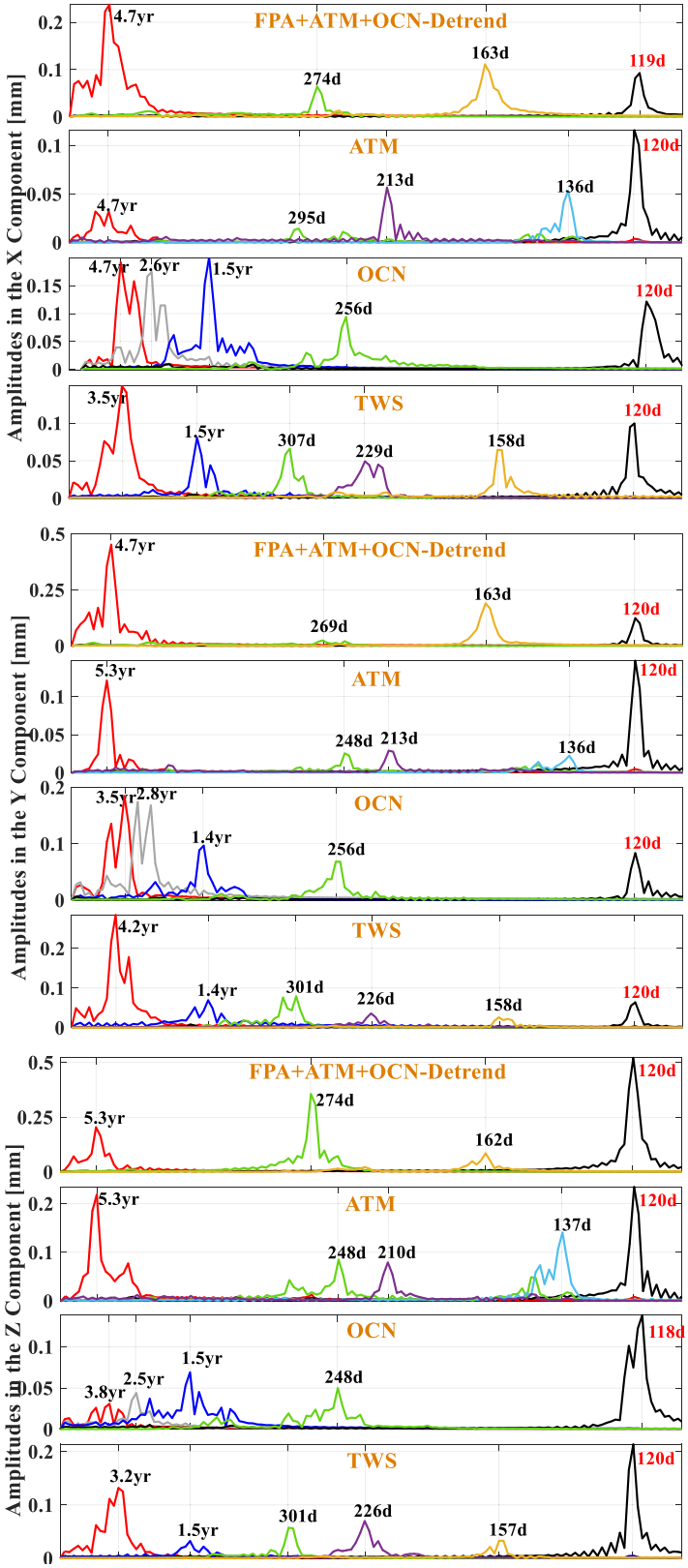

Figure 9. Periodic signals detected by MSSA in GCM components, excluding annual and semi-annual signals. Red indicates a period of 3–5 yr, grey denotes 2.5–2.8 yr, blue corresponds to 1.4–1.5 yr, green represents approximately 250–300 d, purple indicates about 220 d, orange corresponds to about 160 d, light blue represents approximately 140 d and black denotes approximately 120 d.

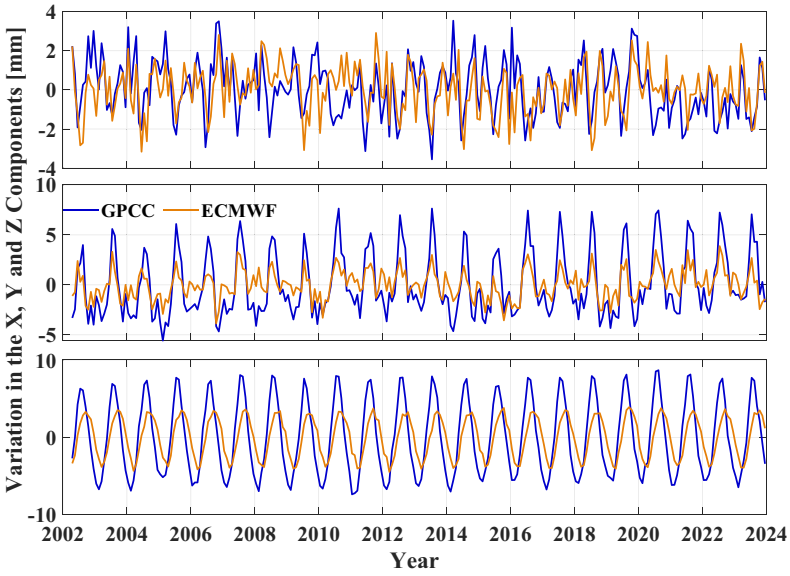

Figure 10. Impact of global precipitation on GCM.

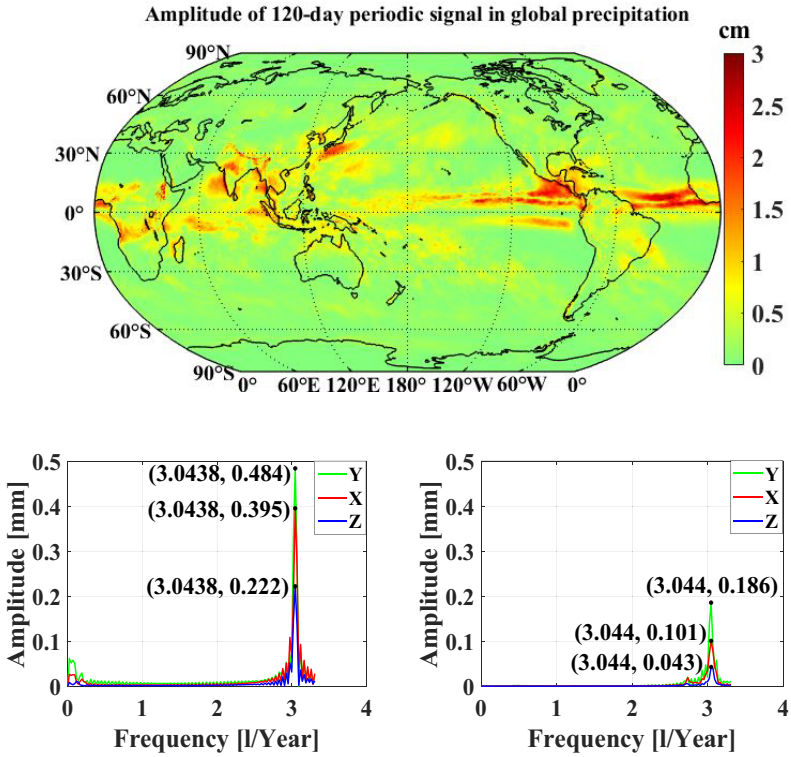

Figure 11. Global amplitude distribution of 120-d signal in ERA5 data (Top) and 120-d periodic signals in precipitation data sets (Bottom left: GPCC, Bottom right: ECMWF).

contrast, the GPCC data set, although based on direct gauge measurements, lacks oceanic coverage and is subject to local topographic effects in data-sparse areas (Schamm *et al.* 2014; Hassler & Lauer 2021; Lavers *et al.* 2022). Further investigation is needed to fully elucidate the causes of these differences.

Both data sets indicate that the amplitude of the ∼120-d signal is largest in the Y component and smallest in the Z component. This suggests a potential connection between ∼120-d precipitation fluctuations and GCM. The stronger ∼120-d signals in the GPCC data compared to ECMWF likely reflect its higher sensitivity in capturing regional precipitation variability, with amplitudes of [0.395, 0.484, 0.222] mm for the X, Y and Z components, respectively, compared to ECMWF's [0.101, 0.186, 0.043] mm. The relatively small amplitude in the Z component indicates that while precipitation fluctuations contribute to GCM variability, other geophysical factors, such as polar ice cap mass changes, likely modulate GCM variations along the Z-axis. To further illustrate the spatial characteristics of the ∼120-d precipitation

variations, we present a global amplitude map based on ECMWF data. The results highlight stronger signals along the Y axis associated with land-based hydrological accumulation, weaker signals along the ocean-dominated X axis and minimal signals in the Z component due to limited high-latitude precipitation fluctuations.

These findings underscore the potential role of ∼120-d periodic precipitation variations in modulating GCM dynamics, offering new insights into sub-seasonal mass redistribution processes in global climate variability and hydrological cycles. Additionally, the ∼120-d periodic signal has also been detected in variations of atmospheric circulation (Stan & Krishnamurthy 2019; Stan 2022), atmospheric angular momentum (Manthos *et al.* 2022) and oceanic angular momentum (Nastula *et al.* 2011). Given that these processes are driven by global mass redistribution, their influence on GCM is evident. These results emphasize the complexity of Earth's mass balance dynamics, highlighting the need for further research to disentangle climate-induced and non-climatic influences on GCM variability.

Furthermore, ENSO has been shown to be closely associated with regional climate variability at subseasonal timescales (Jung & Kirtman 2016; Martineau *et al.* 2021; Park *et al.* 2023; Park & Son 2024), potentially modulating the GCM through its influence on precipitation patterns. Nevertheless, the specific linkage between the ∼120-d signal identified in this study and ENSO remains to be systematically examined and confirmed in future research.

5 DISCUSSION AND CONCLUSION

This study explores the dominant factors influencing seasonal GCM signals using the FPA, with a particular focus on the roles of ATM, OCN and TWS. To address the absence of atmospheric and oceanic contributions in the FPA-derived GCM, the ATM and OCN components were incorporated. Given ongoing uncertainties in glacier mass balance modelling, this study primarily focuses on the major drivers of seasonal variations. Correlations and lag analyses among ATM, OCN, TWS and GCM reveal varying degrees of phase lag among the four series. In both the X and Z components, ATM and OCN lag behind TWS. Notably, TWS exhibits a delayed negative correlation with GCM, peaking at lags of 5–7 month, further reflecting the delayed response of TWS in modulating GCM. However, these lag relationships alone do not fully explain the observed seasonal amplitudes of GCM, particularly in the Z component, where glacier mass changes (GLA and GRE) also contribute substantially.

To further examine amplitude and phase behaviour, MSSA was applied to GCM, ATM, OCN, TWS and their combined time-series. The results reveal strong annual and semi-annual signals across all series, with the annual signal amplitudes significantly exceeding the semi-annual amplitudes. Amplitude differences among components reflect the varying contributions of each driver to seasonal GCM variations. Notably, the GCM and ATM + OCN + TWS series demonstrate high consistency in both amplitude and phase for the annual and semi-annual signals, as reflected by their clear clustering patterns. In contrast, the ATM, OCN and TWS signals are more dispersed, particularly OCN, which shows greater variability. Quantitative variance analysis reveals that TWS is the primary contributor to seasonal GCM variations in the Y and Z components, explaining 66.4 per cent and 67.9 per cent of the variance, respectively. Although the combined contributions of ATM and OCN in the X and Y components are comparable to or exceed those of TWS, they remain significantly lower than TWS in the Z component. The combined ATM + OCN + TWS explains up to 97.9 per cent, 98.1 per cent and 90.8 per cent of the GCM variance in the X, Y and Z components, respectively, confirming their dominant roles as the primary seasonal GCM drivers.

After removing trends, annual and semi-annual signals, MSSA identified additional periodic signals. The analysis detected a spurious ∼140-d signal in the ATM time-series, attributed to high-frequency noise. Meanwhile, ∼160-d periodic signals were detected across all GCM and TWS components, corresponding to half the nodal period of GRACE and GRACE-FO satellites and likely an aliasing artifact. Additionally, ∼120-d periodic signals were discovered in the GCM, ATM, OCN and TWS time-series, indicating the widespread presence of this period in different data sets. To validate the origin of the ∼120-d signal, global precipitation data were analysed using MSSA. The results suggest that this signal contributes to GCM variations in the X, Y and Z components, with the largest amplitude observed in the Y component, likely tied to the spatial distribution of precipitation. In contrast, the smallest amplitude in the Z component indicates that other geophysical factors, such as polar ice cap mass changes, may dominate GCM along this axis. The pervasiveness of the ∼120-d signal highlights how global precipitation patterns redistribute Earth's mass, offering new insights into climate-induced geophysical variations.

While MSSA effectively captures seasonal components, it has limitations in detecting signals beyond this timescale. Kiani Shahvandi *et al*. (2024) demonstrated that core dynamics exert a nonlinear influence on TWS, ice sheet melting and global glacier variations, contributing to approximately 90 per cent of interannual and decadal-scale changes. Given the nonlinearity and complex interactions among multiple geophysical processes, MSSA may not fully capture the overall characteristics of these signals in GCM time-series. To enhance its applicability in Earth system dynamics, future research should focus on refining MSSA for improved detection of interannual and decadal variations. However, this limitation does not affect the study's focus on seasonal variations, which remain the primary scope of this analysis.

In conclusion, this study elucidates the dominant roles of TWS, ATM and OCN as the primary contributors to seasonal GCM variations, with varying influence across components. Notably, the consistent detection of a ∼120-d periodic signal, likely associated with precipitation patterns, underscores the significance of climate-driven mass redistribution in modulating seasonal GCM signals. These results offer a solid foundation for advancing our understanding of Earth's time-variable mass distribution and its geophysical drivers.

ACKNOWLEDGMENTS

This work is primarily supported by the National Natural Science Foundation of China (Project No. 42304099, 42171426), the Natural Science Foundation of Liaoning Province (Project No. 2025-BS-0408), the National Key Research and Development Program of China (Project No. 2025YFE0102700) and the Natural Science Foundation of Henan Province (Project No. 242300420618). The authors thank the editors and anonymous reviewers for their constructive comments, and colleagues for valuable discussions. We acknowledge the Center for Space Research (CSR) for supplying GRACE data and the ICGEM service for access to the Earth gravity field models used for estimating geocentre motion. In addition, the authors thank the European Centre for Medium-Range Weather Forecasts (ECMWF) and the Global Precipitation Climate Centre (GPCC) for providing global precipitation data.

SUPPORTING INFORMATION

Supplementary data are available at *GJIRAS* online.

Please note: Oxford University Press is not responsible for the content or functionality of any supporting materials supplied by the authors. Any queries (other than missing material) should be directed to the corresponding author for the paper.

CONFLICTS OF INTEREST

The authors declare no conflict of interest. The authors confirm that this work is original and has not been published elsewhere, nor is it currently under consideration for publication elsewhere. The manuscript is approved by all authors for publication.

DATA AVAILABILITY

All data used in this study are publicly available. The GRACE Level-2 RL06.2 and AOD1B-derived ATM and OCN data products, were provided by the Center for Space Research (CSR) and the German Research Centre for Geosciences (GFZ), respectively, and can be accessed via the ICGEM portal (https://icgem.gfz-potsdam.de/sl/temporal). Precipitation data were obtained from the ECMWF ERA5 reanalysis (https://cds.climate.copernicus.eu/datasets/reanalysis-era5-single-levels?tab=download), and the GPCC data sets (https://psl.noaa.gov/data/gridded/data.gpcc.html). The fingerprint data bases used in this study are publicly accessible at https://doi.org/10.6084/m9.figshare.27932184.v1.

REFERENCES

Aliabad, F.A., Zare, M., Malamiri, H.G., Pouriyeh, A. & Shahabi, H., 2024. Reconstructing daytime and nighttime MODIS land surface temperature in desert areas using multi-channel singular spectrum analysis[J], *Ecol. Inform.,* **83,** 102830.

Altamimi, Z., Rebischung, P., Collilieux, X., Métivier, L. & Chanard, K., 2023. ITRF2020: an augmented reference frame refining the modeling of nonlinear station motions[J], *J. Geod.,* **97**(5), 47.

Bouillé, F., Cazenave, A., Lemoine, J.M. & Crétaux, J.F., 2000. Geocentre motion from the DORIS space system and laser data to the Lageos satellites: comparison with surface loading data[J], *Geophys. J. Int.,* **143**(1), 71–82.

Bury, G., Zajdel, R. & Sośnica, K., 2025. Correcting geocenter motion in GNSS solutions by combining with satellite laser ranging data[J], *GPS Solut.,* **29**(4), 158.

Chambers, D.P., Wahr, J. & Nerem, R.S., 2004. Preliminary observations of global ocean mass variations with GRACE[J], *Geophys. Res. Lett.,* **31**(13),.

Chen, J., Tapley, B., Seo, K.W., Wilson, C. & Ries, J., 2019. Improved quantification of global mean ocean mass change using GRACE satellite gravimetry measurements[J], *Geophys. Res. Lett.,* **46**(23), 13 984–13 991.

Chen, J.L., Wilson, C.R. & Seo, K.W., 2009. S2 tide aliasing in GRACE time-variable gravity solutions[J], *J. Geod.,* **83,** 679–687.

Chen, J.L., Wilson, C.R., Eanes, R.J. & Nerem, R.S., 1999. Geophysical interpretation of observed geocenter variations[J], *J. geophys. Res.: Solid Earth,* **104**(B2), 2683–2690.

Chen, T.C., Pfaendtner, J., Chen, J.M. & Wikle, C.K., 1996. Variability of the global precipitable water with a timescale of 90–150 days[J], *J. geophys. Res.: Atmos.,* **101**(D5), 9323–9332.

Cheng, M. & Ries, J., 2017. The unexpected signal in GRACE estimates of C20[J], *J. Geod.,* **91**(8), 897–914.

Cheng, M., 2024. An updated estimate of geocenter variation from analysis of SLR data[J], *Remote. Sens.,* **16**(7), 1189.

Clarke, P.J., Lavallée, D.A., Blewitt, G., Van Dam, T.M. & Wahr, J.M., 2005. Effect of gravitational consistency and mass conservation on seasonal surface mass loading models[J], *Geophys. Res. Lett.,* **32**(8), L083065. doi:10.1029/2005GL022441.

Crétaux, J.F., Soudarin, L., Davidson, F.J., Gennero, M.C., Bergé-Nguyen, M. & Cazenave, A., 2002. Seasonal and interannual geocenter motion from SLR and DORIS measurements: comparison with surface loading data[J], *J. geophys. Res.: Solid Earth,* **107**(B12), ETG 16–11-ETG 16-9.

Dobslaw, H., Bergmann-Wolf, I., Dill, R., Poropat, L. & Thomas, M., 2017. A new high-resolution model of non-tidal atmosphere and ocean mass variability for de-aliasing of satellite gravity observations: AOD1B RL06[J], *Geophys. J. Int.,* **211**(1), 263–269.

Dong, D., Dickey, J.O., Chao, Y. & Cheng, M.K., 1997. Geocenter variations caused by atmosphere, ocean and surface ground water[J], *Geophys. Res. Lett.,* **24**(15), 1867–1870.

Dong, D., Yunck, T. & Heflin, M., 2003. Origin of the international terrestrial reference frame[J], *J. geophys. Res.: Solid Earth,* **108**(B4), doi:10.1029/2002JB002035.

Eltahir, E.A. & Bras, R.L., 1996. Precipitation recycling[J], *Rev. Geophys.,* **34**(3), 367–378.

Fallah, A., Sungmin,, O. & Orth, R., 2020. Climate-dependent propagation of precipitation uncertainty into the water cycle[J], *Hydrol. Earth Syst. Sci.,* **24**(7), 3725–3735.

Golyandina, N. & Osipov, E., 2007. The "Caterpillar"-SSA method for analysis of time series with missing values[J], *J. Stat. Plan. Inference,* **137**(8), 2642–2653.

Guo, J., Li, W., Chang, X., Zhu, G. & Liu, X., 2018. Terrestrial water storage changes over Xinjiang extracted by combining Gaussian filter and multichannel singular spectrum analysis from GRACE[J], *Geophys. J. Int.,* **213**(1), 397–407.

Guo, J.Y., Han, Y.B. & Hwang, C.W., 2008. Analysis on motion of Earth's center of mass observed with CHAMP mission[J], *Sci. China Ser. G: Phys. Mech. Astron.,* **51**(10), 1597–1606.

Haines, B., Bertiger, W., Desai, S., Ellmer, M. & Heflin, M., 2024. A global combination of geodetic techniques at the observation level: new perspectives on the terrestrial reference frame[J], *J. geophys. Res.: Solid Earth,* **129**(12), e2024JB029527.

Hassler, B. & Lauer, A., 2021. Comparison of reanalysis and observational precipitation data sets including ERA5 and WFDE5[J], *Atmosphere,* **12**(11), 1462.

Ji, K., Shen, Y., Chen, Q. & Wang, F., 2023. Extended singular spectrum analysis for processing incomplete heterogeneous geodetic time series[J], *J. Geod.,* **97**(8), 74.

Jung, E. & Kirtman, B.P., 2016. ENSO modulation of tropical Indian Ocean subseasonal variability[J], *Geophys. Res. Lett.,* **43**(24), 12,634–612,642.

Kiani Shahvandi, M., Adhikari, S., Dumberry, M., Modiri, S. & Heinkelmann, R., 2024. Contributions of core, mantle and climatological processes to Earth's polar motion[J], *Nat. Geosci.,* **17**(7), 705–710.

Kondrashov, D. & Ghil, M., 2006. Spatio-temporal filling of missing points in geophysical data sets[J], *Nonlinear Process. Geophys.,* **13**(2), 151–159.

Kuang, D., Bar-Sever, Y. & Haines, B., 2015. Analysis of orbital configurations for geocenter determination with GPS and low-Earth orbiters[J], *J. Geod.,* **89,** 471–481.

Kuang, D., Bertiger, W., Desai, S.D., Haines, B.J. & Yuan, D.-N., 2019. Observed geocenter motion from precise orbit determination of GRACE satellites using GPS tracking and accelerometer data[J], *J. Geod.,* **93,** 1835–1844.

Lavers, D.A., Simmons, A., Vamborg, F. & Rodwell, M.J., 2022. An evaluation of ERA5 precipitation for climate monitoring[J], *Q. J. R. Meteorolog. Soc.,* **148**(748), 3152–3165.

Liu, B., Shan, C., Rao, W., Xing, X. & Tan, J., 2024. A GNSS Terrestrial Water Storage Inversion Method Based on GRACE Spatial Constraints[J], *IEEE J. Selected Topics Appl. Earth Obs. Remote Sens.,* **17,** 16487–16496.

Manthos, Z.H., Pegion, K.V., Dirmeyer, P.A. & Stan, C., 2022. The relationship between surface weather over North America and the Mid-Latitude Seasonal Oscillation[J], *Dyn. Atmos. Oceans,* **99,** 101314.

Martineau, P., Nakamura, H. & Kosaka, Y., 2021. Influence of ENSO on North American subseasonal surface air temperature variability[J], *Weather Clim. Dyn.,* **2**(2), 395–412.

Nastula, J., Paśnicka, M. & Kołaczek, B., 2011. Comparison of the geophysical excitations of polar motion from the period: 1980.0–2009.0[J], *Acta Geophys.,* **59,** 561–577.

Nie, Y., Chen, J., Xu, G. & Löcher, A., 2025. Barystatic sea level change observed by satellite gravimetry: 1993–2022[J], *Proc. Natl. Acad. Sci.,* **122**(27), e2425248122.

Otosaka, I.N. *et al.* 2022. Mass balance of the Greenland and Antarctic ice sheets from 1992 to 2020[J], *Earth Syst. Sci. Data,* **2022,** 1–33.

Pan, Y., Zhang, X., Jiao, J., Ding, H. & Shum, C.K., 2025. Geodetic evidence of the interannual fluctuations and long-term trends over the Antarctic ice sheet mass change[J], *IEEE J. Selected Topics Appl. Earth Obs. Remote Sens.,* **18,** 4525–4535.

Park, C.-H., Choi, J., Son, S.-W., Kim, D. & Yeh, S.-W., 2023. Sub-seasonal variability of ENSO teleconnections in Western North America and its prediction skill[J], *J. geophys. Res.: Atmos.,* **128**(6), e2022JD037985.

Park, C.H. & Son, S.W., 2024. Subseasonal variability of ENSO–East Asia teleconnections driven by tropical convection over the Indian ocean and Maritime Continent[J], *Geophys. Res. Lett.,* **51**(13), e2023GL108062.

Peltier, W., Argus, D.F. & Drummond, R., 2018. Comment on "An assessment of the ICE-6G_C (VM5a) glacial isostatic adjustment model" by Purcell et al[J], *J. geophys. Res.: Solid Earth,* **123**(2), 2019–2028.

Rebischung, P., Altamimi, Z., Collilieux, X., Métivier, L. & Chanard, K., 2024. ITRF2020 seasonal geocenter motion model[J], *J. Geod.,* **98**(9), 78.

Ries, J.C., 2016. Reconciling estimates of annual geocenter motion from space geodesy[C], in *Proceedings of the 20th International Workshop on Laser Ranging,* Potsdam, Germany, p. 10–14.

Rietbroek, R., 2014. *Retrieval of Sea Level and Surface Loading Variations from Geodetic Observations and Model Simulations: An Integrated Approach[D],* Rheinische Friedrich-Wilhelms-Universität Bonn, Diss., 2014.

Rietbroek, R., Brunnabend, S.E., Kusche, J. & Schröter, J., 2012. Resolving sea level contributions by identifying fingerprints in time-variable gravity and altimetry[J], *J. Geodyn.,* **59-60,** 72–81.

Rietbroek, R., Brunnabend, S.E., Kusche, J., Schröter, J. & Dahle, C., 2016. Revisiting the contemporary sea-level budget on global and regional scales[J], *Proc. Natl. Acad. Sci.,* **113**(6), 1504–1509.

Schamm, K., Ziese, M., Becker, A., Finger, P. & Meyer-Christoffer, A., 2014. Global gridded precipitation over land: a description of the new GPCC First Guess Daily product[J], *Earth Syst. Sci. Data,* **6**(1), 49–60.

Shen, Y., Wang, F. & Chen, Q., 2021. Weighted multichannel singular spectrum analysis for post-processing GRACE monthly gravity field models by considering the formal errors[J], *Geophys. J. Int.,* **226**(3), 1997–2010.

Sośnica, K., Jäggi, A., Meyer, U., Thaller, D., Beutler, G., Arnold, D. & Dach, R., 2015. Time variable Earth's gravity field from SLR satellites[J], *J. Geod.,* **89,** 945–960.

Stan, C. & Krishnamurthy, V., 2019. Intra-seasonal and seasonal variability of the Northern Hemisphere extra-tropics[J], *Clim. Dyn.,* **53**(7-8), 4821–4839.

Stan, C., 2022. The forecast skill of the Northern Hemisphere middle latitudes seasonal oscillation and its impact on the surface air temperature[J], *Geophys. Res. Lett.,* **49**(4), e2021GL095543.

Sun, Y., Li, Y., Guo, X. & Guo, J.Y., 2023. Estimating C30 coefficients for GRACE/GRACE-FO time-variable gravity field models using the GRACE-OBP approach[J], *J. Geod.,* **97**(3), 20.

Sun, Y., Riva, R. & Ditmar, P., 2016. Optimizing estimates of annual variations and trends in geocenter motion and J2 from a combination of GRACE data and geophysical models[J], *J. geophys. Res.: Solid Earth,* **121**(11), 8352–8370.

Sun, Y., Riva, R., Ditmar, P. & Rietbroek, R., 2019. Using GRACE to explain variations in the Earth's oblateness[J], *Geophys. Res. Lett.,* **46**(1), 158–168.

Swenson, S., Chambers, D. & Wahr, J., 2008. Estimating geocenter variations from a combination of GRACE and ocean model output[J], *J. geophys. Res.: Solid Earth,* **113**(B8),.

Tamisiea, M.E., Hill, E.M., Ponte, R.M., Davis, J.L. & Velicogna, I., 2010. Impact of self-attraction and loading on the annual cycle in sea level[J], *J. geophys. Res.: Oceans,* **115**(C7),.

Tapley, B.D., Bettadpur, S., Watkins, M. & Reigber, C., 2004. The gravity recovery and climate experiment: mission overview and early results[J], *Geophys. Res. Lett.,* **31**(9),.

Tapley, B.D., Watkins, M.M., Flechtner, F., Reigber, C. & Bettadpur, S., 2019. Contributions of GRACE to understanding climate change[J], *Nat. Clim. Change,* **9**(5), 358–369.

Trenberth, K.E., Dai, A., Rasmussen, R.M. & Parsons, D.B., 2003. The changing character of precipitation[J], *Bull. Am. Meteorol. Soc.,* **84**(9), 1205–1218.

Vishwakarma, B.D., Bates, P., Sneeuw, N., Westaway, R.M. & Bamber, J.L., 2021. Re-assessing global water storage trends from GRACE time series[J], *Environ. Res. Lett.,* **16**(3), 034005.

Wu, X., Ray, J. & van Dam, T., 2012. Geocenter motion and its geodetic and geophysical implications[J], *J. Geodyn.,* **58,** 44–61.

Wu, X.P., Heflin, M.B., Ivins, E.R. & Fukumori, I., 2006. Seasonal and interannual global surface mass variations from multisatellite geodetic data[J], *J. geophys. Res.: Solid Earth,* **111**(B9).

Xue, Y. & Lau, W.K.M., 2024. Subseasonal-to-seasonal predictability of extreme precipitation and land forcing[J], *Clim. Dyn.,* **62**(4), 2599–2601.

Yu, H., Sośnica, K. & Shen, Y., 2021. Separation of geophysical signals in the LAGEOS geocentre motion based on singular spectrum analysis[J], *Geophys. J. Int.,* **225**(3), 1755–1770.

Yu, H., Zhang, Y., Sun, Y. & Sośnica, K., 2025a. Unveiling GRACE-based estimation techniques: insights from multichannel singular spectrum analysis of geocentre motion[J], *Geophys. J. Int.,* **242**(1), ggaf002.

Yu, H.J., Liu, W.J., Zhang, L., Sośnica, K. & Wang, J., 2025b. A novel scaling factor correction for GRACE terrestrial water storage anomaly in the Yellow River Basin[J], *J. Hydrol.: Regional Studies,* **59,** 102466. doi:10.1016/j.ejrh.2025.102466.

Zajdel, R., Sośnica, K., Dach, R., Bury, G. & Prange, L., 2019. Network effects and handling of the geocenter motion in multi-GNSS processing[J], *J. geophys. Res.: Solid Earth,* **124**(6), 5970–5989.

Zannat, U.J. & Tregoning, P., 2017. Estimating network effect in geocenter motion: theory[J], *J. geophys. Res.: Solid Earth,* **122**(10), 8360–8375.

Zhang, H. & Sun, Y., 2018. Climate-driven seasonal geocenter motion during the GRACE period[J], *Acta Geophys.,* **66,** 223–232.

Zhang, Y., Zhang, H., Yang, Y., Liu, N. & Gao, J., 2021. Seismic random noise separation and attenuation based on MVMD and MSSA[J], *IEEE Trans. Geosci. Remote Sens.,* **60,** 1–16.

Zhu, Z., Wang, M., Wang, J., Duan, A. & Liu, B., 2025. Intraseasonal oscillation intensity variations of the atmospheric heat source over the Tibetan plateau and their relationship with summer precipitation[J], *J. Clim.,* **38**(4), 931–946.